Original research article

Estimation of microvascular capillary physical parameters using MRI assuming a pseudo liquid drop as model of fluid exchange on the cellular level

Mansour Ashoor[a], Abdollah Khorshidi[b],*, Leila Sarkhosh[a]

[a] *Nuclear Science & Technology Research Institute, P.O. Box: 113653486, Tehran, Iran*
[b] *Cellular and Molecular Research Center, Gerash University of Medical Sciences, P.O. Box: 7441758666, Gerash, Iran*

ARTICLE INFO

ABSTRACT

Aim: One of the most important microvasculatures' geometrical variables is number of pores per capillary length that can be evaluated using MRI. The transportation of blood from inner to outer parts of the capillary is studied by the pores and the relationship among capillary wall thickness, size and the number of pores is examined.

Background: Characterization of capillary space may obtain much valuable information on the performance of tissues as well as the angiogenesis.

Methods: To estimate the number of pores, a new pseudo-liquid drop model along with appropriate quantitative physiological purposes has been investigated toward indicating a package of data on the capillary space. This model has utilized the MRI perfusion, diffusion and relaxivity parameters such as cerebral blood volume (CBV), apparent diffusion coefficient (ADC), ΔR_2 and ΔR_2^* values. To verify the model, a special protocol was designed and tested on various regions of eight male Wistar rats.

Results: The maximum number of pores per capillary length in the various conditions such as recovery, core, normal-recovery, and normal-core were found to be 183 ± 146, 176 ± 160, 275 ± 166, and 283 ± 143, respectively. This ratio in the normal regions was more than that of the damaged ones. The number of pores increased with increasing mean radius of the capillary and decreasing the thickness of the wall in the capillary space.

Conclusion: Determination of the number of capillary pore may most likely help to evaluate angiogenesis in the tissues and treatment planning of abnormal ones.

1.   Background

Some theories have been proposed to recognize the performance of tissues via estimating some microvascular capillary physical parameters. Those may be developed to evaluate tissue metabolism in MRI. Capillaries are a part of cardiovascular system, consisting of single layer endothelial cells, permit rapid exchange of water and solutes with interstitial fluid via the pores created dynamically as ding-dong in the capillary wall, and form an interconnecting network of tubes of different lengths. Capillary density distribution and its geometrical specifications vary from tissue to tissue. In metabolically active tissues the capillaries are numerous, whereas in less active tissues the capillary density is low. Therefore, geometry evaluation of capillaries may be useful in medicine.

The MRI perfusion, diffusion and relaxivity parameters such as cerebral blood volume (CBV), apparent diffusion coefficient (ADC), the differences between relaxation rates pre-contrast and post-contrast agent injection ($\Delta R_2 = R_2 - R'_2$ and $\Delta R^*_2 = R_2 - R'^*_2$ without and with considering magnetic field impurity correspondingly) were using to characterize the microvasculature space. For instance, an approach suggested by Dennie et al.[1] which measures changes in the spin–spin suggested relaxation rates $1/T'_2 = R'_2$ and $1/T'^*_2 = R'^*_2$ caused by the injection of a blood pool restricted contrast agent, are proposed to be sensitive to microvessel density. Van Rijswijk et al.[2] have reported that apparent diffusion coefficient (ADC) values of all tumors, subcutaneous fat, and muscle were significantly higher than true diffusion coefficients, indicating a contribution of perfusion to the ADC. Also, true diffusion measurements, which are corrected for the perfusion effect, have potential to be used as a noninvasive parameter in the characterization of soft-tissue masses. Therefore, in theory, diffusion and perfusion information in MRI maps are combined to obtain morphological information such as mean radius, volume and possibly capillary plasma velocity. Also, the appropriate practical investigations on measuring mean radius of capillary in the various regions of rat brain are presented.

Gambarota et al.,[3] an enhanced contrast method in measuring blood volume have utilized for brain tumors via Gadolinium-DTPA/USPIO agents to distinguish vascular leakage and ultra-small iron oxide particles. Although the defined index in micro- and macro-vasculatures has been characterized, it hast been not estimated by different weighted and b-values. On the other hand, some researchers[4–7] recently have reported the diffusion-weighted imaging (DWI) of soft tissue and musculoskeletal lesions to estimate perfusion fractions to compare with the ADC values. Pekcevik et al.,[4] have determined the mean ADC amounts by single-shot echoplanar imaging technique using a 1.5 T MRI device that some overlap have reported between benign and malignant tumors. In this study, combination of diffusion and perfusion maps including capillary density, volume, capillary plasma velocity, CBV, ADC and the differences between relaxation rates before and after contrast-agent injection is utilized to determine the relation among mean radius, number of pores and wall thickness of capillary in four different regions. To differentiate normal from abnormal domains, the corrected perfusion effect can be scrutinized by a new method called pseudo-liquid drop model.

2.   Aim

A combined model is suggest to confirm a package of data on geometrical parameters and an essential way in transportation of blood from inner to outer parts of the capillary. It is utilized from CBV, ADC, ΔR_2 and ΔR^*_2 values to calculate the number of pores per capillary length. The aim is to estimate mean radius, length and capillary density in normal and abnormal regions by introducing pseudo-diffusion coefficient.

3.   Materials and methods

3.1.   Theory

One may estimate the mean capillary radius (r_c) by using the CBV, ADC, ΔR_2 and ΔR^*_2 values as follows,[8,9]

$$r_{c(\mu m)} = \left(7.57 \times 10^3 \, \frac{D.CBV}{Vol_{(voxel)}} \cdot \frac{\Delta R_2^{*2}}{\Delta R_2^3} \right)^{0.5} \tag{1}$$

where D is diffusion constant of water.[10,11] The residence time of blood in a capillary is also only on the order of 1–2 s. Therefore, each capillary may only support a very small volume of tissue in which the blood pass from the capillary thickness as pseudo-liquid drops based on twofold permeable process. The capillary lumen lies within a circumferential ring of several endothelial cells, as shown in Fig. 1. The endothelium is perforated by numerous small holes called fenestrae which are considered for passing blood as pseudo-liquid drop. The fenestrae are sometimes covered by a thin membrane that provides selectivity with regard to the size of solutes that are allowed to pass through. The flow of charged molecules through channels in the cell membrane is responsible for the creation of the membrane potential. Solute transport occurs both through bulk fluid motion and by solute diffusion due to the presence of solute concentration gradients. The diffusion of a solute will also be affected by the presence of a variety of heterogeneous structures. Solutes will need to diffuse through porous structures such as the capillary wall, around or through cells within the extravascular space, and through the interstitial fluid containing a variety of macromolecules.[12] In general, the transport of essential water soluble molecules across the cell membrane is achieved through the use of special transmembrane proteins that have a high specificity for a
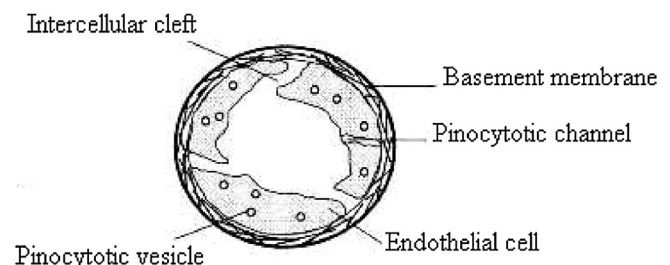

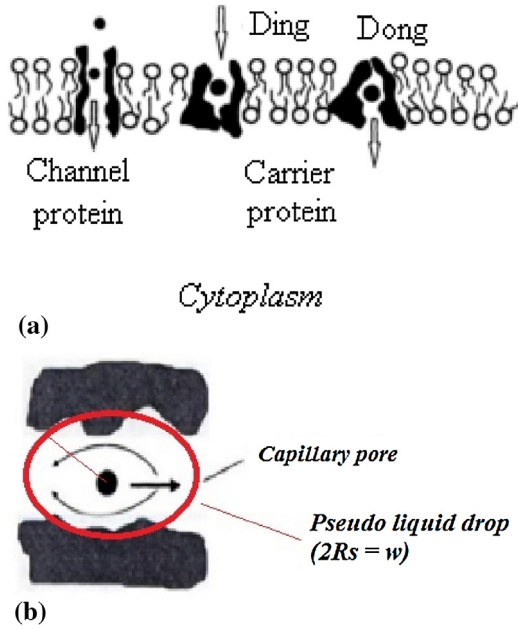**Fig. 1 – Cross section diagram of a capillary[12] [p. 104].**

(a)

(b)

Fig. 2 – (a) Membrane transport proteins. Carrier protein exists in two conformational states, "ding" and "dong"[12] [p. 113]. (b) Solvent flows across solute in small pores increases drag[12] [p. 205].

certain type or class of molecules. There are two basic types of membrane transport proteins, carrier proteins and channel proteins. The carrier proteins bind to the solute and then undergo a change in shape or conformation ("ding" to "dong") that allows the solute to traverse the cell membrane to be named as pseudo-liquid drop here. The carrier protein therefore changes between two shapes, alternately presenting the solute-binding site to either site of the membrane. Channel proteins actually form water-filled pores that penetrate across the cell membrane. Solutes that cross the cell membrane by either carrier or channel proteins are said to be passively transported.[12] Thus, in this study, it is supposed that blood moves into tissue from capillary as pseudo-liquid drops with a shape of *spherical* with mean radius of R_S approximately which sphere volume is as $4.189 R_S^3$, as shown in Fig. 2. Assuming in the steady state situation and under common conditions, the fraction of *all blood* in the capillary (α) is in the *pores* of the capillary wall, one may obtain the following formula,

$$3 \times \alpha \times (r - R_S)^2 \times l = 4 \times n_p \times R_S^3 \qquad (2)$$

where n_p and r are the number of pores on the capillary wall and capillary radius, respectively. The α parameter is a constant value at the ranges 0 through 1. Also, in this model, one may suppose that the $2 \times R_S = \omega$ value is the *wall thickness* of capillary due to connectivity and disconnectivity endothelial cells. Thus, the number of pores per length is as follows,

$$\frac{n_p}{l} = \frac{3\alpha(2r - \omega)^2}{2 \times \omega^3} \qquad (3)$$

Alternatively, the number of the pores per total capillary surface area (TCSA) is defined as follows,

$$\frac{n_p}{TCSA} = \frac{n_p}{2\pi(r - \omega/2) \times l} = \frac{3\alpha(2r - \omega)}{2\pi \times \omega^3} \qquad (4)$$

Besides, the mean capillary diameter is very larger than the wall thickness ($2r \gg \omega$), so $2r - \omega \approx 2r$. Rewriting Eqs. (3) and (4), one may obtain,

$$\frac{n_p}{l} \cong 45.42 \times 10^3 \frac{\alpha}{\omega^3} \frac{D.CBV}{Vol_{(voxel)}} \cdot \frac{\Delta R_2^{*2}}{\Delta R_2^3} \qquad (5)$$

$$\frac{n_p}{TCSA} = \frac{\alpha}{\omega^3} \left(6.9 \times 10^3 \frac{D.CBV}{Vol_{(voxel)}} \cdot \frac{\Delta R_2^{*2}}{\Delta R_2^3} \right)^{0.5} \qquad (6)$$

The number of pores per capillary length and per the total capillary surface area will be maximum while $\alpha = 1$. It may be assumed that $\alpha = 1$, because the capillaries' radii are very small approximately $2.5\,\mu m$ and the wall thickness is almost $0.5\,\mu m$. Therefore, one may obtain $0.4 \times r = 2 \times \omega$ which indicates approximately the volume of *all blood* in the capillary is the same as that of in the capillary wall.

3.2. MRI measurement procedure

To evaluate the proposed theory and develop a test protocol, the following measurement was made on various vasculature regions of eight male Wistar rats using a 7 T MRI system. Briefly, an aged white clot (prepared 24 h before ischemia) was slowly injected into the internal carotid artery to block the middle cerebral artery (MCA).[13,14] All animal experiments were carried out in accordance with National Institutes of Health guide for the care and use of Laboratory animals (NIH Publications No. 8023, revised 1978). MRI measurements were performed using a 7 T, 20 cm bore super conducting magnet (Magnex Scientific, Abingdon, UK) interfaced to a SMIS console (Surrey, England). A 12-cm bore actively shielded gradient coil set; capable of producing magnetic field gradients up to $20E-4T/cm$ was used. The radio frequency (RF) pulses were applied by a 7.5 cm diameter saddle coil actively decoupled by transistor–transistor logic (TTL) control from the 1.4 cm surface receive coil which was positioned over the center line of the animal skull. Stereotaxic ear bars were used to minimize movement during the imaging procedure. During MRI measurements, anesthesia was maintained using a gas mixture of N_2O (69%), O_2 (30%) and halothane (1%). Rectal temperature was kept at $37 \pm 0.5\,°C$ using a feedback controlled water bath.

A modified fast low angle shot (FLASH)[15] imaging sequence was employed for reproducible positioning of the animal in the magnet at each MRI session.[16–18] Diffusion weighted imaging (DWI) and perfusion weighted imaging (PWI) measurements were performed at 24 h after onset of embolization.

The spin–spin relaxation time (T_2) was measured by using standard two-dimensional Fourier transform (2DFT) multi-slice (seven slices) multi-echo (four echo) MRI. A series of four sets of images (7 slices for each set) were obtained using echo times (TE) of 20, 40, 60, and 80 ms and a repetition time (TR) of 3 s. Images were produced using a 32 mm field of view (FOV), 2 mm slice thickness, and 128×64 image matrix. The

total time for the entire sequence was approximately 3.2 min. Transverse relaxation rates, R_2^*, R_2', and R_2 $(1/T_2^*$, $1/T_2'$, and $1/T_2)$, were measured by using the Look-Locker sequence[19] which provides the data required to construct multi-section maps of R_2^*, R_2', and R_2 in a single acquisition.[19–21] For this study, five gradient echoes, with a first echo time of 10 ms and an inter-echo spacing of 8 ms, were acquired prior to the 180° pulse. The echo train after the 180° pulse contained six echoes separated by 8.1 ms. A series of eleven sets of images (7 slices for each set) were obtained using TEs of 98 ms and a TR of 3 s. Images were produced using a 32 mm FOV, 2 mm slice thickness, and 128 × 128 image matrix. The total time for the entire sequence was approximately 6.4 min.

ADC_w was measured by using the Stejskal–Tanner sequence with three b-values (10, 800, and 1800 s/mm^2) in each of three diffusion sensitizing directions, seven slices, 32 mm FOV, 128 × 64 matrix size, TR = 1.5 s and TE = 40 ms. Each image required a scan time of 3.2 min for completion. The total time for the entire sequence was approximately 14.4 min.

Perfusion measurements were performed prior to each diffusion measurement by using arterial spin tagging technique.[22–24] Two images were obtained for perfusion measurement with parameters, TR = 1 s, TE = 30 ms, 64 × 64 image matrix, 3 mm slice thickness, and a 32 mm FOV. In animal PWI was measured within a coronal section, with coordinates centered at interaural 8.2 mm and bregma 0.8 mm.[25–28] The duration of the inversion pulse was 1 s at a B1 amplitude with a frequency of 0.3 kHz. The volume of voxel was 0.3125 × 0.3125 × 2 mm^3 here.

4. Results

In this study, it was suggested a pseudo-liquid drop model during blood transport along with appropriate quantitative physiological purposes for determination of the number of pores per capillary length in various regions using MRI. Fig. 3 depicts the obtained practical maps (MTT, ADC, CBV, CBF, ΔR_2 and ΔR_2^*) utilizing noise reduction and artifact cancelation algorithms. Using the ROIs in the various regions on the maps, the perfusion and diffusion parameters have been measured. Table 1 indicates the amounts of T_2, ADC, ΔR_2^*, ΔR_2, MTT, CBF, CBV, r, and Np/l in the eight rats as mean ± S.D. The maximum number of pores per capillary length in the four regions such as recovery, core, normal-recovery, and normal-core were found to be 183 ± 146, 176 ± 160, 275 ± 166, and 283 ± 143, respectively. These results demonstrated that the number of pores per capillary length in the normal regions is more than that of the damaged ones.
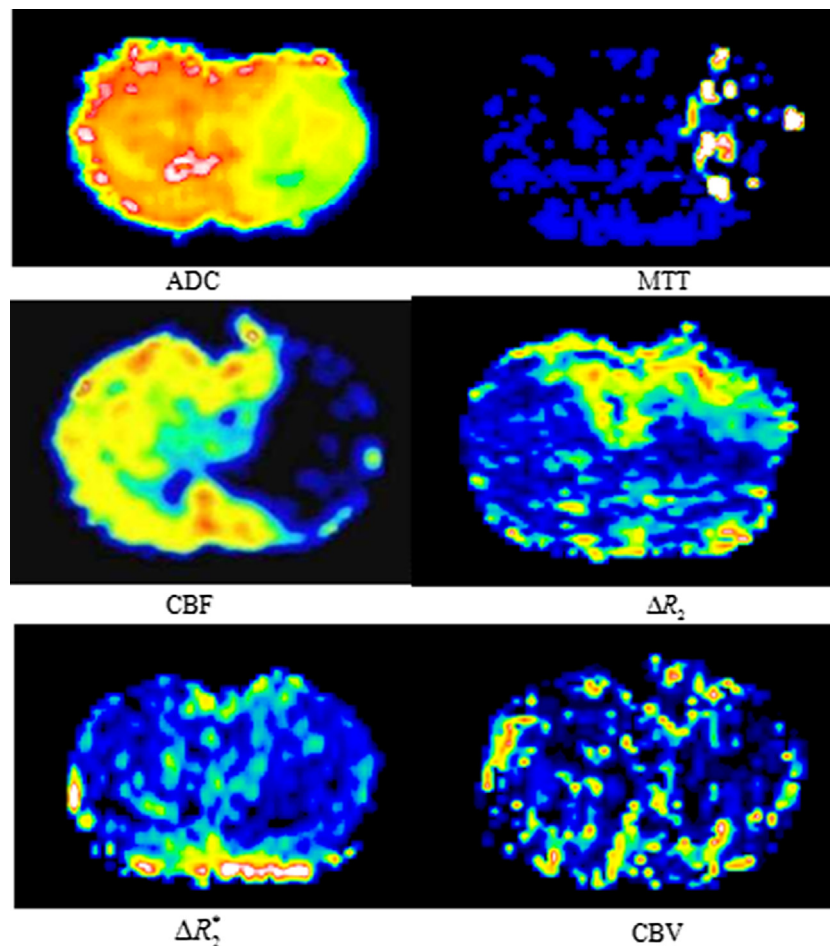

Fig. 3 – ADC, CBF, MTT, ΔR_2, ΔR_2^* and CBV maps. Left side of all images is normal, and selected ROIs are based on the right side that is a damaged region.

Table 1 – Measured and calculated values of various parameters at the different regions of the rats for $n = 8$ at capillary wall thickness value of $w = 0.5\,\mu m$ and $\alpha = 1$ (mean $\pm$ S.D.).				
	Recovery	Core	Normal-recovery	Normal-core
T_2 (s)	59.62 ± 11.60	44.96 ± 16.30	54.17 ± 4.16	55.8 ± 6.54
ADC $\times 10^{-4}$ (mm^2/s)	8.96 ± 1.95	2.22 ± 0.46	7.87 ± 0.9	7.89 ± 0.97
ΔR_2^* (1/s)	14.87 ± 6.23	14.40 ± 5.21	14.12 ± 6.03	13.85 ± 5.38
ΔR_2 (1/s)	7.15 ± 1.36	4.87 ± 1.64	6.95 ± 1.23	7.03 ± 1.08
MTT (s)	3.54 ± 1.49	2.94 ± 0.87	5.21 ± 3.15	5.37 ± 3.67
CBV	0.91 ± 0.5	0.93 ± 0.54	1.75 ± 0.96	1.87 ± 0.91
r (μm)	1.86 ± 1.49	1.79 ± 1.63	2.8 ± 1.69	2.88 ± 1.46
n_p/l ($w = 0.5$)	183.38 ± 146.55	175.78 ± 160.35	275.52 ± 166.29	283.59 ± 143.16

The mean capillary radius has been verified through microscopy methods and in various published material on this subject.[29–36] Pathak et al.[30] showed that in normal contra-lateral section of the brain, the mean microvasculature radius was $3.72 \pm 0.72\,\mu m$. Also, for instance, the ADC values of normal cortex and caudate-putamen were $(726 \pm 22) \times 10^{-6}$ mm^2/sand $(659 \pm 17) \times 10^{-6}$ mm^2/s, respectively.[37] These, however, are approximately in agreement with the results obtained from this study.

With respect to the values 0.01 through 0.1 for $CBV/Vol_{(voxel)}$ parameter and 1 through 1000 s for $\Delta R_2^{*2}/\Delta R_2^3$, the mean radius of capillary using Eq. (1) in theory section has been varied from 0.076 to 7.58 μm. Fig. 4 depicts the relationship among mean capillary radius, $CBV/Vol_{(voxel)}$ and CSSRT parameters where CSSRT is $\Delta R_2^{*2}/\Delta R_2^3$ value with the two different diffusion constants of water as 0.0007 mm^2/s and 0.0004 mm^2/s. As shown, with increasing the diffusion constant of water, the mean capillary radius increases.

According to Eq. (3) in theory, the number of pores per capillary length increases with decreasing the capillary wall thickness. Besides, Eq. (4) indicates that the number of the pores per the total capillary surface area increases with decreasing the capillary wall thickness. Experimentally, the number of pores per capillary length is indicated as a function of the mean radius and capillary wall thickness in Fig. 5. The constant parameter of α is 1 here. The number of pores per capillary length will increase with increasing the mean radius as well as decreasing the wall thickness.

5. Discussion

This manuscript focuses on estimating the number of pores. A new pseudo-liquid drop model along with appropriate quantitative physiological purposes has been investigated toward indicating a package of data on the capillary space. This model has utilized the MRI perfusion, diffusion and relaxivity parameters such as cerebral blood volume (CBV), apparent diffusion coefficient (ADC), ΔR_2 and ΔR_2^* values.[17] The wall of a capillary consists of a single layer of endothelial cells that are surrounded on their outside by a basement membrane. In general, the basement membrane is about 50–100 nm thick. The capillaries are very small, having radii of about 2.5 μm and a length which is less than 0.3 mm, and the total thickness of the capillary wall is about 0.5 μm which are in agreement with the results approximately here, as indicated in Table 1. Ungersma et al.,[38] have been shown correlations between in vivo vascular MRI and ex vivo structural vessel measurements so that
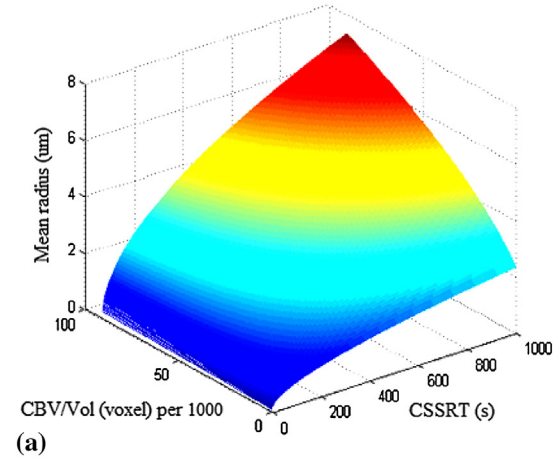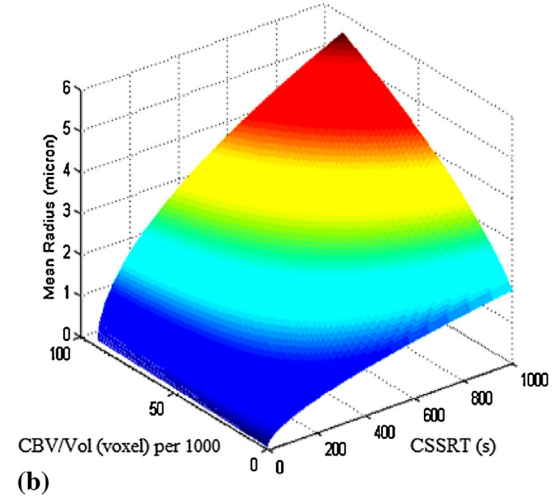

Plot of mean radius of capillary in the normal region with D = 0.0007 mm^2/s

(a)

Plot of mean radius of capillary in the normal region with D = 0.0004 mm^2/s

(b)

Fig. 4 – Plots showing the relationship between mean capillary radius, $CBV/Vol_{(voxel)}$ and CSSRT parameters where CSSRT is $\Delta R_2^{*2}/\Delta R_2^3$ value with the diffusion constant of water (a) 0.0007 mm^2/s and (b) 0.0004 mm^2/s. As shown, with increasing the diffusion constant of water, the mean capillary radius increases.

the viable tumor segmentation increased sensitivity for detection of significant effects on blood volume (reduction by 18 and 36) and vessel density (reduction by 33 and 52) at 48 h post-treatment from two antiangiogenic therapeutics. Here, the mean radius and the number of capillary pores were
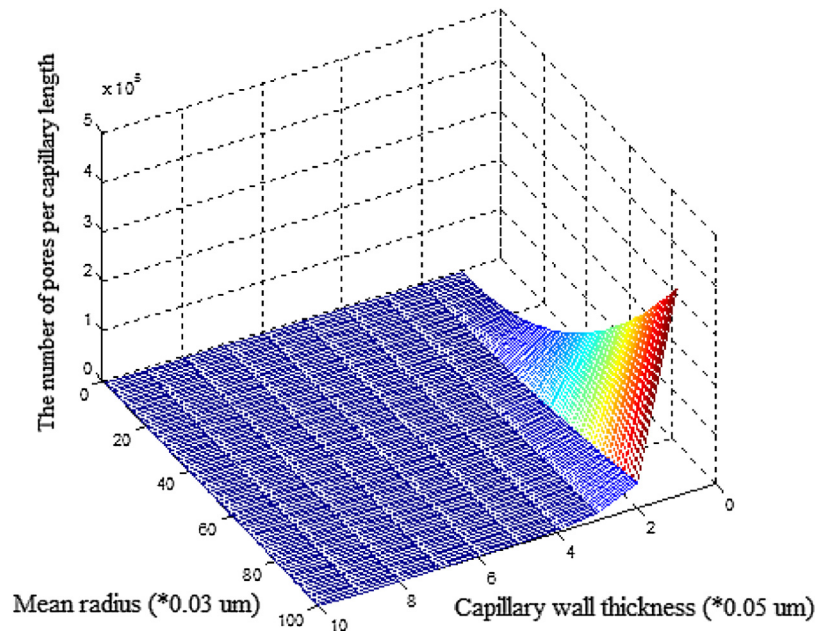
Fig. 5 – The maximum number of pores per capillary length is indicated as a function of the mean radius and capillary wall thickness because the constant parameter of α is 1 here. The number of pores per capillary length will increase with increasing the mean radius and decreasing the wall thickness.

dependent on the ADC, CBV and $\Delta R_2^{*2}/\Delta R_2^3$ and wall thickness. Quantity $\Delta R_2^{*2}/\Delta R_2^3$ plays a major role in quantification of dynamic and static specifications of capillaries in perfusion and diffusion MRI.[39] As this quantity was increased, for a constant $CBV/Vol_{(voxel)}$ in capillary space, mean capillary radius was also increased. Such increase will accelerate as $CBV/Vol_{(voxel)}$ was further increased. The maximum (minimum) mean radius occurs when $\Delta R_2^{*2}/\Delta R_2^3$ and $CBV/Vol_{(voxel)}$ were both maximized (minimized).

Energy depletion, temperature, intracellular water accumulation, changes in tortuosity of the extracellular diffusion paths and changes in cell membrane permeability have all been implicated as contributing to the changes in ADCw. The increase in ADCw appears to occur concomitantly with loss of membrane structure and loss of barriers to diffusion. The decreased ADCw is associated with a specific threshold level of regional cerebral blood flow, similar to that which is associated with the loss of membrane potential, and is also associated with breakdown of energy metabolism, acidosis, cellular ionic shifts, and decreased Na+, K+-ATPase activity. Background imaging gradients, gradient linearity, refocusing RF pulses, eddy currents, image misregistration, noise and dynamic range contribution as systemic sources of errors, may affect estimation of ADC value. Also, microscopic, biophysical tissue properties, partial volume effects, anisotropy, restriction, diffusion distance, compartmentation, exchange, multiexponential diffusion decay, T_2 weighting and microvascular perfusion are responsible for ADC inaccuracy.[11,40–43] They affect estimation of static and dynamic specifications of capillary, not in the scope of this study.

Some important factors and mechanisms such as intercellular cleft, vesicles, neutral molecules, plasma proteins, hydrodynamic effects, osmotic pressure, pinocytosis, solute radius, steric exclusion, tortuosity, plasmapheresis, hydraulic conductance, heterogeneous materials, hydrophobic molecules, and sieving coefficient affect the number of pores per capillary length. Komlosh et al.,[44] have demonstrated pore diameters were agree with pore sizes using two methods in optical microscopy and single/double pulsed-filed-gradient diffusion diffraction NMR spectroscopy. Also, Douma et al.,[9] have shown that the tumor blood volume in estimating vessel size was 4-fold lower with 7 T MRI than with laser scanning method, whereas muscle blood volume was comparable. The R_2^* and R_2 parameters in regions adjacent to large and small vessels have a different behaviors so that their changes ratio are relevant to the average dimension of the micro-vessels. Furthermore, Bredno et al.,[45] have simulated blood and contrast agent dynamics as a combination of convection and diffusion in tubular networks by cerebral arterial and microvascular model. The obtained curves were nearly so that the defined vascular dispersion operator and retention function had been evaluated. In this study, these mechanisms that allow for the transport of solutes across the capillary wall based on the pseudo-liquid drop model are the intercellular cleft and pinocytotic vesicles and channels.

The intercellular cleft is a thin slit or slit-pore that is formed at the interface between adjacent endothelial cells. The size of thin slit is about 6–7 nm, just sufficient to retain albumin and other larger proteins. The collective surface area of these openings represents less than 0.001 of the total capillary surface area which is proportional with the number of pores per capillary length. In general, the driving force for the passive transport of solutes is due to the combined effect of their concentration gradient and the electrical potential difference that exists across the membrane. Neutral molecules diffuse from regions of high concentration to regions of low concentration.

However, if the molecule carries an electrical charge, then both the concentration gradient and the electrical potential difference, or voltage gradient, across the cell membrane will affect the transport of the molecule. The electrochemical gradient is the term used to describe the combined effect of charge and solute concentration on the transport of a molecule which is related to the pseudo-liquid drop model. Also, the ADC of Na$^+$ is mostly influenced by motion in the extracellular space and Na$^+$ can be observed as a reporter molecule for motion in that space. The water ADC is dominated by intracellular motion as well.[46]

The plasma proteins are generally larger than the capillary slit-pores. Although ellipsoid-shaped proteins, for example the clotting protein fibrinogen, may have a minor axis that is smaller than that of the capillary slit-pore, the streaming effect caused by the fluid motion within the capillary orients the major axis of the proteins parallel to the flow axis and prevents their entry into the slit-pore. Therefore, the smaller substances found in the plasma, such as ions, glucose, and metabolic waste products, will readily pass through the slit-pores of the capillary wall, whereas the plasma proteins will be retained in the lumen of the capillary. Since the plasma proteins are the only constituent of the plasma that does not readily pass through the capillary wall, it is the plasma proteins that are responsible for the formation of the osmotic pressure between the interstitial and plasma fluids. The colloid osmotic pressure is actually quite small in comparison to the osmotic pressure that is developed when a cell is placed in pure water. In this case, it is assumed that all of the species present within the intracellular fluid are retained by the cell membrane. The flow of fluid across the capillary wall or a porous membrane is driven by a difference in pressure across the capillary wall or membrane. This pressure difference arises not only from hydrodynamic effects but also from the difference in osmotic pressure between the fluids separated by the membrane. Approximately 90% of the fluid that leaves at the arterial end of the capillary is reabsorbed at the venous end. However, the 10% that is not reabsorbed by the capillary collects within the interstitium and enters the lymphatic system that these parameters affect the α value in Eq. (2). Furthermore, lipid-soluble substances such as oxygen and carbon dioxide can diffuse directly through the endothelial cells that line the capillary wall without the use of the slit-pores. In addition to the slit-pores, there are two other pathways that can provide additional routes for the transport of large lipid-insoluble solutes such as proteins across the endothelium of the capillary wall. These pathways are called pinocytosis and receptor-mediated transcytosis.[47] The receptor-mediated transcytosis can provide for significant transport of specific solutes across the capillary endothelium. The ligand–receptor complexes are endocytosed forming transcytotic vesicles. These vesicles are either processed internally or they can move through the cell and reattach themselves to the opposite side of the cell. The transcytotic vesicle then releases its contents by exocytosis. In many cases in pore diffusion, the solute radius is also comparable to that of the pore radius. This leads to two additional effects, both reducing the diffusion rate of the solute. The first effect, called steric exclusion, restricts the ability of the solute from entering the pore from the bulk solution. Therefore, only a fraction of the pore volume is available to the molecule. Because of steric exclusion, the equilibrium concentration of solute is less within the pore mouth than in the bulk solution. As the solute molecule diffuses through the pore, it experiences hydrodynamic drag caused by the flow of solvent over the surface of the solute, as shown in Fig. 2b. As the solute radius increases relative to that of the pore radius, this hydrodynamic drag increases, reducing or restricting the diffusion of the solute through the pore compared to its motion in the bulk fluid.

Some of the blood plasma that enters the capillary will be carried or filtered across the capillary wall by the combined effect of the hydrodynamic and oncotic pressure differences that exist between the capillary and the surrounding interstitial fluid. The heterogeneous materials affect solute diffusion. There are the types of solute diffusivity such as the diffusivity within the pores of the capillary wall. For solute transport across the capillary wall, one must consider that the available surface area is not the total surface area, but the pore area. This assumes that the solute itself is not soluble in the continuous nonporous phase. Furthermore, the solute must follow a path through the pores that is more tortuous, making the diffusion distance greater than the thickness of the membrane. Obviously, a great of pores exist on the capillaries for passing blood into tissue which these pores vary dynamically from geometrical specification point of view.

Furthermore, the perfusion of the plasma across the capillary wall will carry with it a variety of solutes that are present in the blood. Because of the size of the pores in the capillary wall, this filtration of the plasma by the capillary wall will also tend to separate the solutes on the basis of their size.

Discontinuous capillaries have large endothelial cell gaps that readily allow the passage of proteins, and even red blood cells. Solute transport through the capillary wall as a representative porous semipermeable membrane is considered. The cell membrane is impermeable to polar or other water-soluble molecules. Hence, large neutral polar molecules like glucose have very low cell membrane permeabilities. Charged molecules and ions such as H$^+$, Na$^+$, K$^+$, and Cl$^-$ also have very low permeabilities. Hydrophobic molecules, such as oxygen and nitrogen, readily dissolve in the lipid bilayer and show very high permeabilities. Smaller neutral polar molecules such as CO_2, urea, and water, are able to permeate the lipid bilayer because of their much smaller size and neutral charge. These parameters have a key role on the number of pores per capillary length.

In this study, it was suggested a pseudo-liquid drop model along with suitable quantitative physiological purposes for determination of the number of pores per capillary length in various regions using MRI. This model was utilized as an essential way in transportation of blood from inner to outer parts of the capillary. The number of pores per capillary length in the normal regions was more than that of the damaged ones. Finally, the number of pores increased with increasing mean radius of capillary as well as decreasing the wall thickness. At present, there is no technique for measuring the number of pores on the capillary wall for comparing with the obtained results of the theory. Perhaps this subject will be evaluated by using smart nano-materials as contrast agents which injected into the vessel. The microvasculature geometrical features on capillary wall thickness, the size and number of

pores could be scrutinized by precise specification via relation among CBV, ADC, ΔR_2 and ΔR_2^*. By completing the pseudo-liquid drop model and considering other components and variables, there might be another way to achieve comprehensive method. The corrected diffusion via weighted and various b-values need to more investigated in estimation of perfusion fraction within normal and abnormal parts.

6. Conclusions

The evaluation of microvasculature space by MRI may provide more information about tissues to demonstrate their function and to choice the best approach in treatment planning. The number of pores per capillary length and pore sizes can be increased by accumulation of proteins because protein–protein interactions strengthen cell wall supporting expansion. The discrimination among various lesions in mapping ADC needs knowing the potential causes of biochemical parameters apart from cellular evidences. Also, examples of changes in blood transportation and different contrast agents can be instrumental in examining the number of capillary pores.

Conflict of interest

None declared.

Financial disclosure

None declared.

Acknowledgements

REFERENCES

1. Dennie J, Mandeville JB, Boxerman JL, Packard SD, Rosen BR, Weisskoff RM. NMR imaging of changes in vascular morphology due to tumor angiogenesis. *Magn Reson Med* 1998;**40**:793–9.
2. Van Rijswijk CSP, Kunz P, Hogendoorn PCW, Taminiau AHM, Doornbos J, Bloem JL. Diffusion-weighted MRI in the characterization of soft-tissue tumors. *J Magn Reson Imaging* 2002;**15**:302–7.
3. Gambarota G, Leenders W, Maass C, et al. Characterisation of tumour vasculature in mouse brain by USPIO contrast-enhanced MRI. *Br J Cancer* 2008;**98**:1784–9.
4. Pekcevik Y, Kahya MO, Kaya A. Characterization of soft tissue tumors by diffusion-weighted imaging. *Iran J Radiol* 2015;**12**(3):1–6.
5. Rijswijk CSP, Kunz P, Hogendoorn PCW, Taminiau AHM, Doornbos J, Bloem JL. Diffusion-weighted MRI in the characterization of soft-tissue tumors. *J Magn Reson Imaging* 2002;**15**:302–7.
6. Nagata S, Nishimura H, Masafumi Uchida M, et al. Diffusion-weighted imaging of soft tissue tumors: usefulness of the apparent diffusion coefficient for differential diagnosis. *Radiat Med* 2008;**26**:287–95.
7. Subhawong TK, Jacobs MA, Fayad LM. Insights into quantitative diffusion-weighted MRI for musculoskeletal tumor imaging. *Am J Roentgenol* 2014;**203**:560–72.
8. Ashoor M, Jiang Q, Chopp M, Jahed M. Introducing a new definition towards clinical detection of microvascular changes using diffusion and perfusion MRI. *Sci Iranica* 2005;**12**:109–15.
9. Douma K, Oostendorp M, Slaaf DW, Post MJ, Backes WH, Zandvoort AMJ. Evaluation of magnetic resonance vessel size imaging by two-photon laser scanning microscopy. *Magn Reson Med* 2010;**63**:930–9.
10. Yankeelov TE, Pickens DR, Price RR. In: Hendee WR, editor. *Quantitative MRI in cancer*. Rochester, MN: Taylor, Francis; 2011. p. 165–73.
11. Tropres I, Grimault S, Vaeth A, et al. Vessel size imaging. *Magn Reson Med* 2001;**45**:397–408.
12. Fournier RL. *Basic transport phenomena in biomedical engineering*. CRC Press; 2011. p. 111–3, third edition. Taylor & Francis, Boca Raton. Chapter 5, pp.: 175–179 and chapter 3.
13. Zhang L, Zhang RL, Jiang Q, Ding D, Chopp M, Zhang ZG. Focal embolic cerebral ischemia in the rat. *Nat Protoc* 2015;**10**(4):539–47.
14. Zhang R, Chopp M, Zhang Z, Jiang Q, Ewing JR. A rat model of embolic focal cerebral ischemia. *Brain Res* 1997;**766**:83–92.
15. Haase A, Frahm J, Matthaei D, Hänicke W, Merboldt KD. FLASH imaging: rapid NMR imaging using low flip angle pulses 1986. *J Magn Reson* 2011;**213**:533–41.
16. Jiang Q, Zhang ZG, Chopp M, et al. Temporal evolution and spatial distribution of the diffusion constant of water in rat brain after transient middle cerebral artery occlusion. *J Neurol Sci* 1993;**120**:123–30.
17. Wang L, Yushmanov VE, Liachenko SM, Tang P, Hamilton RL, Xu Y. Late reversal of cerebral perfusion and water diffusion after transient focal ischemia in rats. *J Cereb Blood Flow Metab* 2002;**22**(3):253–61.
18. Bhaskar S, Stanwell P, Cordato D, Attia J, Levi C. Reperfusion therapy in acute ischemic stroke: dawn of a new era? *BMC Neurol* 2018;**18**(1):1–26.
19. Ma J, Wehrli FW. Method for image-based measurement of the reversible and irreversible contribution to the transverse-relaxation rate. *J Magn Reson B* 1996;**111**:61–9.
20. Cheng HLM, Stikov N, Ghugre NR, Wright GA. Practical medical applications of quantitative MR relaxometry. *J Magn Reson Imaging* 2012;**36**:805–24.
21. Sedlacik J, Boelmans K, Löbel U, Holst B, Siemonsen S, Fiehler J. Reversible, irreversible and effective transverse relaxation rates in normal aging brain at 3 T. *Neuroimage* 2014;**84**:1032–41.
22. Williams D, Detre J, Leigh J, Koretsky A. Magnetic resonance imaging of perfusion using spin inversion of arterial water. *Proc Natl Acad Sci USA* 1992;**89**:212–6.
23. Ferré JC, Bannier E, Raoult H, Mineur G, Carsin-Nicol B, Gauvrit JY. Arterial spin labeling (ASL) perfusion: techniques and clinical use. *Diagn Interv Imaging* 2013;**94**(12):1211–23.
24. Pollock JM, Tan H, Kraft RA, Whitlow CT, Burdette JH, Maldjian JA. Arterial spin labeled MRI perfusion imaging: clinical applications. *Magn Reson Imaging Clin N Am* 2009;**17**(2):315–38.
25. Paxinos G, Watson C. *The rat brain in stereotaxic coordinates*. 7th ed. New York: Academic Press, Elsevier; 2013.
26. Aggarwal M, Zhang J, Miller MI, Sidman RL, Mori S. Magnetic resonance imaging and micro-computed tomography combined atlas of developing and adult mouse brains for stereotaxic surgery. *Neuroscience* 2009;**162**(4):1339–50.
27. Li X, Aggarwal A, Hsu J, Jiang H, Moria S. AtlasGuide: software for stereotaxic guidance using 3D CT/MRI hybrid atlases of

developing mouse brains. *J Neurosci Methods* 2013;**220**(1):75–84.

28. Lu H, Scholl CA, Zuo Y, et al. Registering and analyzing rat fMRI data in the stereotaxic framework by exploiting intrinsic anatomical features. *Magn Reson Imaging* 2010;**28**(1):146–52.

29. Bihan DL, Turner R. The capillary network: a link between IVIM and classical perfusion. *Magn Reson Med* 1992;**27**:171–8.

30. Pathak AP, Schmainda KM, Ward BD, Linderman JR, Rebro KJ, Greene AS. MR-Derived cerebral blood volume maps: issues regarding histological validation and assessment of tumor angiogenesis. *Magn Reson Med* 2001;**46**:735–47.

31. Gesztelyi G, Finnegan W, DeMaro JA, Wang J, Chen J, Fenstermacher J. Parenchymal microvascular systems and cerebral atrophy in spontaneously hypertensive rats. *Brain Res* 1993;**611**:249–57.

32. Lin SZ, Sposito N, Pettersen S, et al. Cerebral capillary bed structure of normotensive and chronically hypertensive rats. *Microvasc Res* 1990;**40**:341–57.

33. Dunn JF, Roche MA, Springett R, et al. Monitoring angiogenesis in brain using steady-state quantification of with MION infusion. *Magn Reson Med* 2004;**51**:55–61.

34. Triantafyllou A, Anyfanti P, Pyrpasopoulou A, Triantafyllou G, Aslanidis S, Douma S. Capillary rarefaction as an index for the microvascular assessment of hypertensive patients. *Curr Hypertens Rep* 2015;**17**:33.

35. Calcinaghi N, Wyss MT, Jolivet R, et al. Multimodal imaging in rats reveals impaired neurovascular coupling in sustained hypertension. *Stroke* 2013;**44**:1957–64.

36. Biancardi VC, Son SJ, Ahmadi S, Filosa JA, Stern JE. Circulating angiotensin II gains access to the hypothalamus and brain stem during hypertension via breakdown of the blood–brain barrier. *Hypertension* 2014;**63**:572–9.

37. Hoehn-Berlage M, Norris DG, Kohno K, Mies G, Leibfritz D, Hossmann KA. Evolution of regional changes in apparent diffusion coefficient during focal ischemia of rat brain: the relationship of quantitative diffusion NMR imaging to reduction in cerebral blood flow and metabolic disturbances. *J Cerebr Blood F Met* 1995;**15**:1002–11.

38. Ungersma SE, Pacheco G, Ho C, et al. Vessel imaging with viable tumor analysis for quantification of tumor angiogenesis. *Magn Reson Med* 2010;**63**:1637–47.

39. Jensen JH, Chandra R. MR imaging of microvasculature. *Magn Reson Med* 2000;**44**:224–30.

40. Ashoor M, Khorshidi A. Estimation of the number of compartments associated with the apparent diffusion coefficient in MRI: the theoretical and experimental investigation. *Am J Roentgenol* 2016;**206**:455–62.

41. Jiang Q, Chopp M, Zhang ZG, et al. The temporal evolution of MRI tissue signatures after transient middle cerebral artery occlusion in rat. *J Neurol Sci* 1997;**145**:15–23.

42. Welch KMA, Windham J, Knight RA, et al. A model to predict the histopathology of human stroke using diffusion and T2-weighted magnetic resonance imaging. *Stroke* 1995;**26**:1983–9.

43. Conturo TE, McKinstry RC, Aronovitz JA, Neil JJ, Diffusion MRI: precision accuracy and flow effects. *NMR Biomed* 1995;**8**:307–32.

44. Komlosh ME, Özarslan E, Lizak MJ, et al. Pore diameter mapping using double pulsed-field gradient MRI and its validation using a novel glass capillary array phantom. *J Magn Reson* 2011;**208**:128–35.

45. Bredno J, Olszewski ME, Wintermark M. Simulation model for contrast agent dynamics in brain perfusion scans. *Magn Reson Med* 2010;**64**:280–90.

46. Goodman J, Kroenke CD, Bretthorst GL, Ackerman JJ, Neil JJ. Sodium ion apparent diffusion coefficient in living rat brain. *Magn Reson Med* 2005;**53**(5):1040–5.

47. Woodroffe PJ, King JR, Varley CL, Southgate J. Modelling cell signalling and differentiation in the urothelium. *Bull Math Biol* 2005;**67**(2):269–389.